

A Magnetic Particle Imaging Approach for Minimally Invasive Imaging and Sensing with Implantable Bioelectronic Circuits

Zhiwei Tay, Han-Joon Kim, John S. Ho, and Malini Olivo

Abstract—Minimally-invasive and biocompatible implantable bioelectronic circuits are used for long-term monitoring of physiological processes in the body. However, there is a lack of methods that can cheaply and conveniently image the device within the body while simultaneously extracting sensor information. Magnetic Particle Imaging (MPI) with zero background signal, high contrast, and high sensitivity with quantitative images is ideal for this challenge because the magnetic signal is not absorbed with increasing tissue depth and incurs no radiation dose. We show how to easily modify common implantable devices to be imaged by MPI by encapsulating and magnetically-coupling magnetic nanoparticles (SPIOs) to the device circuit. These modified implantable devices not only provide spatial information via MPI, but also couple to our handheld MPI reader to transmit sensor information by modulating harmonic signals from magnetic nanoparticles via switching or frequency-shifting with resistive or capacitive sensors. This paper provides proof-of-concept of an optimized MPI imaging technique for implantable devices to extract spatial information as well as other information transmitted by the implanted circuit (such as biosensing) via encoding in the magnetic particle spectrum. The 4D images present 3D position and a changing color tone in response to a variable biometric. Biophysical sensing via bioelectronic circuits that take advantage of the unique imaging properties of MPI may enable a wide range of minimally invasive applications in biomedicine and diagnosis.

Index Terms—Magnetic Particle Imaging, Implantable Device, Wireless, Bioelectronic Circuits, Reconstruction.

*Zhiwei Tay and Han-Joon Kim contributed equally. Manuscript received Jun 9 2023; revised Nov 20 2023. This work was supported by grants from the Agency of Science, Technology and Research (A*STAR) under its BMRC Central Research Fund (UIBR, Dr. Tay Zhiwei) and Career Development Fund (202D800036) and by the Ministry of Health's National Medical Research Council under its Open-Fund Young Investigator Research Grant (MOH-001142-01). This work was partly supported by the National Research Foundation of Korea (NRF) grant funded by the Korea government (MSIT) (RS-2023-00214390).

Z. Tay was with the Institute of Bioengineering and Bioimaging (IBB), Agency for Science, Technology and Research (A*STAR), Republic of Singapore. He is now with the National Institute of Advanced Industrial Science and Technology, 1-2-1 Namiki, Tsukuba, Ibaraki 305-8564, Japan (e-mail: zhiwei.tay@aist.go.jp).

H.J. Kim, was with the National University of Singapore Department of Bioengineering. He is now with Kumoh National Institute of Technology (e-mail: hanjoonk@kumoh.ac.kr).

John S. Ho is with the Department of Electrical and Computer Engineering and the Institute for Health Technology at the National University of Singapore (email: johnho@nus.edu.sg).

M. Olivo is with the Institute of Materials Research and Engineering (IMRE), Agency for Science, Technology and Research (A*STAR), 2 Fusionopolis Way, Innovis 08-03, Singapore 138634, Republic of Singapore (e-mail: malini.olivo@imre.a-star.edu.sg).

I. INTRODUCTION

MAGNETIC Particle Imaging (MPI) is a nascent imaging modality [1], [2] that directly detects and images magnetic nanoparticles. These may be used within a living subject and safely imaged by MPI to obtain biodistribution data. Because it only detects nanoparticles it benefits from tracer-like contrast with nanomolar sensitivity [3], [4], is linearly quantitative with nanoparticle mass [5], suffers no signal attenuation by tissue thickness, and has zero ionizing radiation dose due to its typical superparamagnetic iron oxide (SPIO) imaging agent [6], [7]. Some important applications of MPI include stem cell tracking [5], cancer imaging [8], acute gut bleed detection [9], lung imaging [10], [11] and stroke and brain imaging [12], [13]. Other examples are cardiovascular imaging [14], real-time surgical instrument steering [15], and image-guided hyperthermia-therapy [16], [17].

Advances in miniaturization of circuit components and biocompatible coatings have made implantable sensor circuits possible in recent years. Such circuits have been used for a myriad of applications from detecting wound dehiscence in internal sutures used for anastomotic procedures [18] to glucose monitoring in deep tissue spaces [19], [20]. The advantage of these microdevices over contrast agent-based biosensors is the much higher sensitivity, wider range of possible sensing targets, and long-term durability and persistence deep within the human body. On the other hand, contrast agent methods tend to have limitations in what metrics they can sense and have much shorter *in vivo* lifespans if biodegradable. One of the key challenges in ultrasmall deep tissue implants is providing external power to them since onboard battery powering proves to be extremely bulky. Both near and far-field approaches have been developed with varying success. Transmission of the collected sensor data to an external receiver using minimal power is another challenge [21].

In view of the above challenges, non-invasive imaging modalities would be a compelling candidate because they are already designed to probe and extract information at deep tissue spaces. Therefore we sought to adapt the deep tissue implant into an imaging agent with the sensor information encoded into the imaging signal. With this strategy, it is possible to harness the imaging mechanism to both power the implant as well as well enable transmission of information outwards without the need for any onboard batteries. In addition, imaging methods offer (1) deeper operational range than

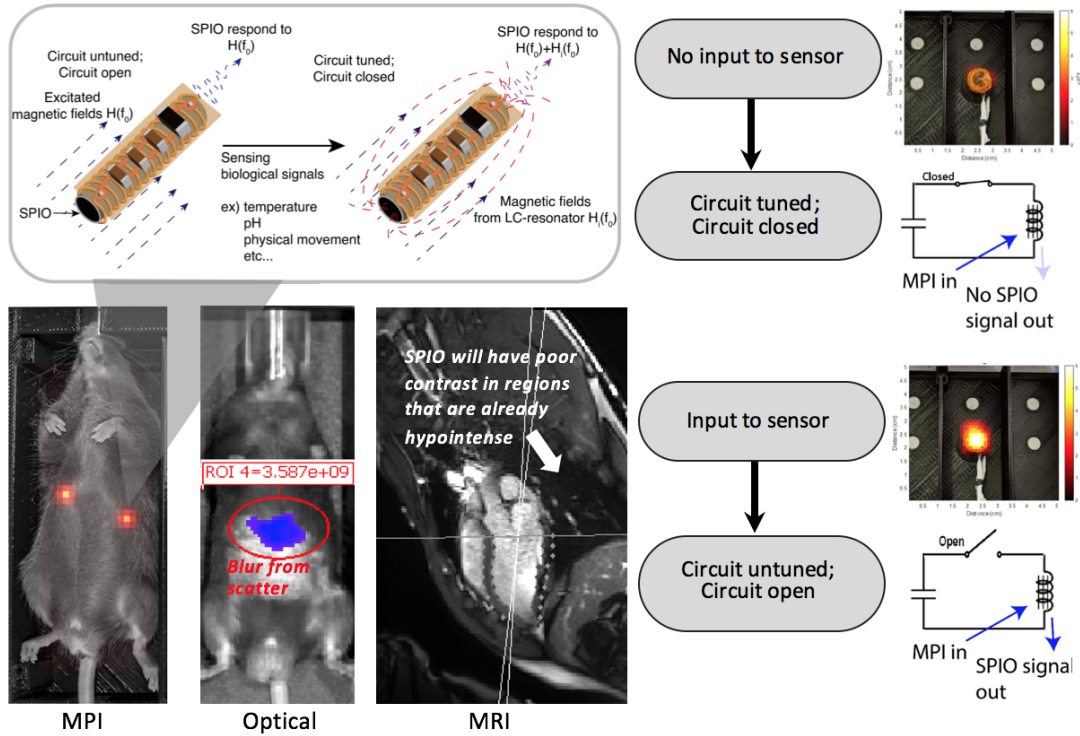


Fig. 1. MPI in conjunction with SPIO-nanoparticle-embedded implantable bioelectronic circuits as a new class of probes for functional MPI measurements. For brevity, we will abbreviate these devices as NPIC (NanoParticle Implantable Circuits) (left) As a new magnetic imaging modality working on different principles from MRI, MPI enables high-sensitivity imaging of implanted probes at-depth *in vivo* while optical-based probes have to contend with blurring from scatter and significant attenuation with tissue depth. Unlike MRI, MPI provides hotspot imaging where the location of the implanted probe is clearly visible and any modulation of the probe signal can be directly measured because there is no MRI background signal that may mask the probe signal. In contrast, SPIO hypointense spots in MRI have poor contrast when located in already hypointense regions of background tissue. Representative images of MPI, optical and MRI are shown here to illustrate these contrasting characteristics. (right) Without input to the sensor, the NPIC circuit is in its tuned or closed-circuit state. Inductive coupling between the MPI scanner's main excitation transmit coil operating at f_0 and the implanted microcircuit coil (top right) electromagnetically shields the SPIO nanoparticle from MPI excitation, suppressing the received MPI signal. On the other hand, input to the sensor detunes, breaks, or adds resistance into the NPIC circuit, reducing the shielding effect of the circuit on the SPIOs and thereby enhancing the received MPI signal. Conveniently, this implies that the MPI probes only 'light up' when the sensor detects an abnormal state, making it useful in massed arrays of implantables where the clinician can quickly focus on areas where probes light up (indicates abnormal biological state).

existing near-field powering strategies, (2) provision of spatial information for a distributed array of identical implanted sensors where frequency-based barcoding may not be ideal and finally (3) spatial tracking of mobile implanted circuits such as wireless untethered microrobots in the gastrointestinal tract, lung or vascular system.

The use of imaging methods for microimplants is not entirely new. Recent work by the Jasanoff lab at MIT has shown the potential of using implantable bioelectronics circuits in tandem with existing imaging methods [22]. Their study focused on a magnetic resonance imaging (MRI) approach, where they demonstrated modulation of the local MRI signal in response to electrical or photonic cues. In another study, sensor-equipped steerable microrobots was shown where the sensor detuning modulates its hyperintensity in the MRI image [23]. In addition, passive and active catheter circuits have been proposed for MRI-based interventional imaging. Susil et al. demonstrated a two-wire electrophysiology (EP) catheter that simultaneously records the intracardiac electrogram and receives the MR signal for active catheter tracking [24]. Bilgin et al. developed a MRI-tuned self-resonating RF microcircuit for *in situ* temperature sensing during interventional MRI. The

sensor has a hyperintense signal in MR images that attenuates with increasing local temperature [25]. Besides MRI, X-ray compatible sensors have also been investigated in prior work on implantable x-ray-based blood pressure microsensor for coronary stent monitoring [26] and X-ray visualized sensors detecting infection within the peritoneal dialysis catheter [27].

These existing modalities described above each have their limitations. Optical methods only work well for shallow implants while MRI methods heavily rely on device contrast with the tissue background and may experience susceptibility artefacts in the MRI image due to the device. Ultrasound methods face challenges in coupling existing sensors to a change in acoustic index as well as the inability to be placed in acoustically-shadowed body regions. MPI, in contrast, suffers no such limitation as magnetic fields penetrate deeply and uniformly through air, bone, and tissue; working well in lungs [11] and the gastrointestinal tract [9]. It also has tracer-like contrast and produces the same signal regardless of tissue background. However, to-date, no study has investigated the potential of MPI for minimally invasive imaging and communication with implantable bioelectronic circuits.

In this work, we demonstrate that MPI has the potential

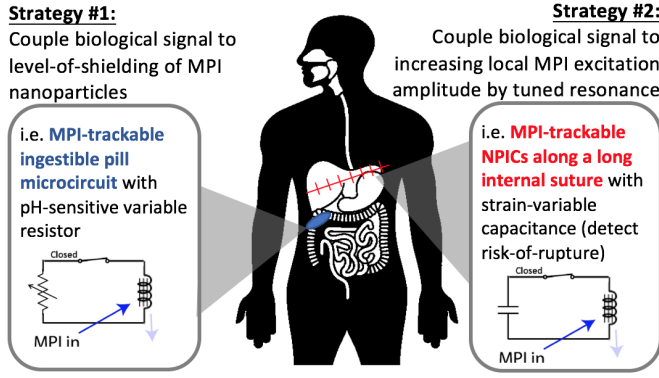


Fig. 2. Strategies to couple the MPI signal to bioelectronic circuit readout. Strategy 1 is to use variable resistors sensitive to biological readouts such as pH and temperature can modulate the amount of shielding the SPIOs in the NPIC receive from the MPI drive field and therefore modulate the MPI signal from a known amount of SPIOs in the device. Strategy 2 is to use tuned resonant circuits with variable capacitors sensitive to biological readouts such as strain can modulate the local MPI f_0 excitation via tuned resonance to increase the magnetic field on the SPIOs locally. In the case of a full rupture leading to an open-circuit, there will be zero modulation of 'felt' drive field by the SPIO which can be clearly distinguished from tuned and de-tuned cases.

to provide spatial information as well as transmit sensor information encoded within the magnetic particle spectrum which we can display as an image color tone (i.e. red for high temperature, blue for low temperature), as shown in Fig. 1. Furthermore, we elaborate on how we modify the MPI imaging approach to enable implanted circuits to encode information into the imaging signal. In particular, unlike MRI or radiation-based modalities, we demonstrate a handheld MPI imaging probe that has the potential to be cheaper or smaller-sized as it does not utilize expensive cryogenics like MRI nor radiation shielding like Computerized Tomography (CT) or X-ray [28]. This zero-radiation-dose, handheld imaging probe is especially suitable for frequent monitoring of the implanted sensor.

This study will be relevant to MPI systems designers as well as implantable sensor designers to develop improved sensor strategies to advance the capabilities of both bioelectronic sensings as well as the expanding application scope of the new imaging modality MPI.

II. THEORY

The general working theory of MPI has been extensively detailed in prior work [1], [29], [30]. To briefly introduce MPI's working principles, MPI utilizes a low frequency (1–45 kHz) drive field combined with strong electromagnetic gradient coils in the background to produce a sensitive low-field region surrounding a null point in the middle of a strong (> 1 T/m) magnetic field gradient. The null point is rastered [30] around the field-of-view or moved in a Lissajous trajectory [1], producing a nonlinear magnetization response at harmonics of the drive carrier frequency as MPI signal from the SPIO nanoparticles when it passes through them. These higher harmonics of the MPI signal are recorded and reconstructed by system matrix or x-space methods into a 3D MPI image that quantitatively shows the spatial distribution of SPIO nanoparticles in the field-of-view (FOV).

A. Coupling of MPI signal to bioelectronic circuit signal readout

The MPI signal from the SPIO nanoparticles can be modulated by the circuit sensor via several avenues such as (1) change in excitation amplitude and (2) change in excitation frequency.

We will focus on the first avenue in this work. There are two strategies illustrated in Fig. 2 to achieve the requisite (1) change in excitation amplitude. The bioelectronic circuit can modulate the incoming excitation (drive) magnetic field from MPI scanner through an inductive shielding mechanism where the strength of the shielding can be modulated by a variable resistor in series with the inductive shield wrapped around the SPIO nanoparticle capsule. The second strategy, a resonant approach, would also be viable as MPI uses a monotonic excitation of the SPIO nanoparticles, and thus the mechanism would rely on shifting the resonant circuit off-resonance to reduce the amount of current flowing and thereby the shielding. This resonant approach will typically increase, rather than reduce the incoming magnetic excitation from the MPI scanner, in a mechanism not unlike resonant inductive coupling. This increases the generated magnetic flux in the secondary coils (the implanted bioelectronic resonant circuit) if it is on-resonant and is strongly modulated by shifting the circuit off-resonance which will dramatically decrease the power transferred and thus the local magnetic flux felt by the SPIO nanoparticles.

B. 3D imaging theory for non-rotating external MPI reader (FFL) to extract both position and sensor-readout information

In the field of implanted sensors, data transmission typically involves the use of a small external reader device that communicates with the implant at near or mid-field. As such, although our proof-of-concept implies that our sensors could be useable by any MPI scanner design (regular inner-bore like MRI, newer open-bore or single-sided designs, etc.), we sought to modify the MPI imaging setup to be more similar to the small external reader context widely used for implanted devices (Fig. 3). While a handheld reader setup will have poorer sensitivity and resolution than the existing larger and more complex MPI scanner designs [34]–[36], we leverage the benefits of being able to have a high concentration of SPIOs within the implanted device remaining undiluted *in vivo* unlike typical blood volume MPI applications, effectively giving us ideal imaging point sources to compensate for the lower performance of reader device. It must be noted that at extremely high concentrations, some nanoparticles such as ResovistTM have been shown to deviate from linearity of signal with tracer mass due to interparticle dipole-dipole interactions beyond a threshold concentration [37]. As such, for our proposed NPIC devices, it is important to ensure that all implanted devices have the same concentration of tracer. We verify this with a baseline calibration of the nanoparticle signal from each device with the shielding turned off such that the equality of signal across all devices can be assured.

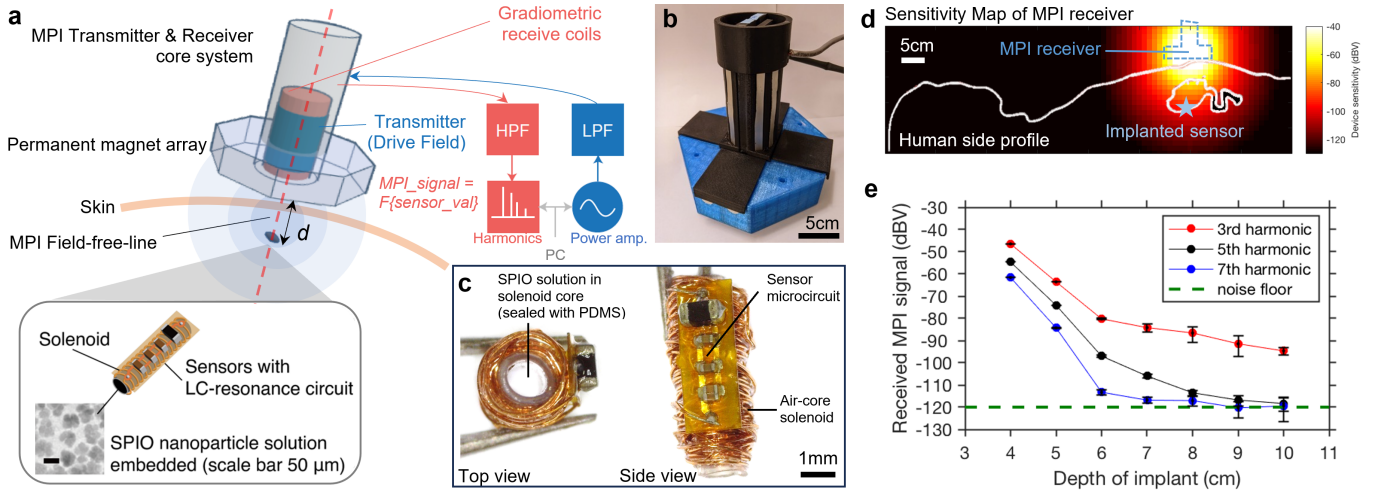


Fig. 3. MPI system and NPIC design and performance. (a) Illustration of the MPI imaging setup of the implanted NPIC sensor within the body. The MPI transmitter sends a low-frequency alternating magnetic field and detects the nanoparticle magnetization response as a magnetic harmonic spectrum modulated by the microcircuit sensors. (b) Photograph of the MPI system based on prior validated MPI system [31]–[33] core transmitter and receiver with the addition of external permanent magnet array for generation of a selection field with a field-free-line geometry. (c) Photograph of the implanted circuit which is an air-core solenoid filled with MNPs connected to R and/or C components on a microcircuit chip. (d) Contour heat map of MPI sensitivity with silhouette of human profile overlaid, with black set to the value of noise floor to delineate undetectable regions. Sensitivity is higher than typical *in vivo* MPI because the entire SPIO dose is concentrated within a small point source (implanted device). (e) Imaging system sensitivity with depth shows the noise floor is reached at 9 cm through tissue where both 3rd and 5th harmonic are just above the noise floor. Two detectable harmonics are needed to provide at least one harmonic ratio to reconstruct for both the imaging X , Y , Z coordinates (from *a priori* known-SPIO-mass) and the ‘color’ information resulting from activity of the sensor circuit on the nanoparticles. Since additional dynamic range is needed for shielding-based ‘encoding’, 7 cm is the more conservative depth-limit to provide this buffer.

The MPI imaging setup used in this study differs from existing single-sided MPI devices [35] and seeks to tailor the imaging to fixed point sources for 4D imaging (3D position + harmonic-based ‘color’ dimension). Generally, the setup is based on a Z -oriented FFL selection field geometry projected from the external reader device into the living subject lying supine in the XY plane (Fig. 3a). At this point, a two-dimensional projection scan can be achieved by simple XY (mechanical) translation of the FFL across the FOV. In order to acquire the Z -coordinate information without having to rotate the MPI scanner or imaged subject through a large number of angles as per standard projection MPI utilizing reconstruction from-projection-angles, our strategy is to harness priors such as the known mass of implanted SPIO and the fact that the drive field weakens with Z -depth. This is highlighted in Fig. 3e, where the signal intensity of higher harmonics (7th harmonic) decreases faster with distance from MPI scanner compared to lower harmonics (3rd harmonic) because the SPIO experiences a drop-off of drive field strength with distance. This results in a predictable change in the ratio of higher-to-lower harmonics with Z -depth. Thus, we harness this to reconstruct the Z -coordinate to obtain the 3D position of our ‘point sources’ in the MPI image.

However, a more complex reconstruction has to be considered to decouple Z -coordinate encoding from sensor encoding since the implanted circuit encodes sensor info via modulating the incoming drive field locally through a small shielding coil or resonant coil around the SPIO point source. First, considering real-life applications, we assume it is reasonable that there is a finite number of devices where there exists a projection XY plane angle such that there is only one device

per Z -line (see Fig. 4). The problem then regresses to the simultaneously solving for both the Z -position and sensor readout r value of a single device. Note that r couples to a shielding or resonant factor affecting the SPIOs via a calibrated function $S(r)$.

Overall, the image reconstruction workflow proceeds as per the following stages: **1) XY -reconstruction, first pass MPI: 2D projection image with FFL along the z -axis** Since the 2D image reconstruction proceeds as per projection x -space MPI reconstruction, the relevant imaging equation for MPI signal $s(\mathbf{x}_s(t))$ is similar to Goodwill et al. [38] as follows:

$$s(\mathbf{x}_s(t)) = B(z) \cdot m\rho_2(\mathbf{x}) * \dot{\mathcal{L}}(kG\mathbf{x}) \cdot \left. \frac{(H_0\omega_0)}{H_{sat}} \right|_{\mathbf{x}=\mathbf{x}_s(t)} \quad (1)$$

where $\mathbf{x}_s(t)$ is the instantaneous position of the FFL in the X, Y coordinates, $B(z)$ [T/A] is the sensitivity value of the MPI receiver coil along the FFL. Since the FFL and MPI receiver coil are moved together mechanically as shown in Figure 3a, the only sensitivity variation is in z due to drop-off by distance in z away from the coil. $m[\text{Am}^{-2}]$ is the nanoparticle magnetic moment, and $\dot{\mathcal{L}}(kG\mathbf{x})$ represents the first derivative of the Langevin function without consideration of velocity of the FFL unlike typical x -space theory because the drive excitation is along the FFL-axis aligned to the z -axis. The FFL only moves sideways in $x-y$ directions, hence the term on the right of the convolution operator is just a calibrated 2D point-spread-function based on the parameters of nanoparticle characteristics k , gradient field G [T/m], and a fixed drive field amplitude H_0 and drive field frequency ω_0 normalized to the saturation field of the SPIO, H_{sat} . Lastly,

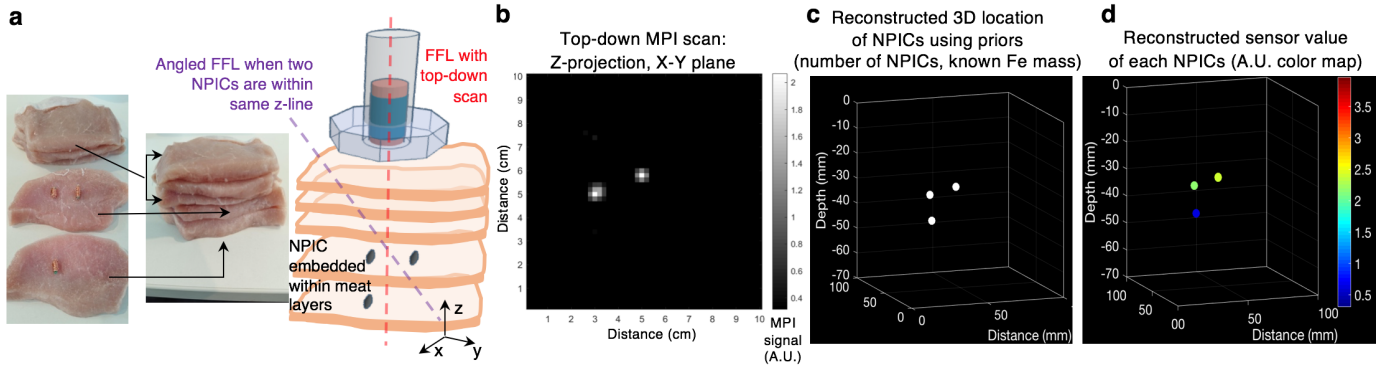


Fig. 4. MPI imaging methodology and performance using layers of meat with implanted devices as a tissue phantom (a) Photo and illustration of imaging phantom setup. Upon detection of multiple implants in the same Z-line, the FFL was angled to an appropriate projection plane where there is only one implant per Z-line as required by theory for the reconstruction of both 3D location and NPIC sensor value. (b) Standard projection MPI image with the red FFL orientation illustrated in panel a, with a resolution of about 5 mm at 2.8 T/m gradient which is sufficient for implants measuring about 5–7 mm in the longest dimension. In this event of multiple implants within the same Z-line. The projection axis of imaging was angled thereafter to purple FFL orientation, enabling 3D reconstruction in panel c. (c) Recovery of depth information from higher harmonics and reconstructed 3D location of each NPIC utilizing powerful priors such as known total number of NPIC and fixed (known, calibrated) iron mass per NPIC. Since every NPIC has the same SPIO mass, there is no need to display concentration information, unlike a standard MPI scan. (d) Recovery of sensor information from the MPI signal as detailed in our reconstruction algorithm in the theory/methods section. The information, for example, temperature, can be represented as a color map as shown.

$\rho_2(\mathbf{x})$ is the projection of the nanoparticle density along the FFL (aligned to z) which can be expressed as an integral of the 3D nanoparticle density in z .

$$\rho_2(x, y) = \int \rho(x, y, z) dz \quad (2)$$

1b) Adjust the angle of the XY imaging plane to ensure a maximum of one NPIC per pixel and repeat step 1.

Since n , the total number of implanted NPIC, is known, the algorithm checks at a coarse resolution if the count of pixels above a threshold intensity value α , is equal to n :

$$\sum_{i=1}^N \frac{s(\mathbf{x}_i) > \alpha}{|s(\mathbf{x}_i)|} \longleftrightarrow n \quad (3)$$

2) Calculating z-coordinate of the sole NPIC in pixel: Obtain ‘felt’ H-field

With [X,Y] coordinates of each NPIC obtained, the reconstruction now switches to a 1D calculation of the z -coordinate only for pixels with NPIC present. We assume non-interacting SPIOs, zero background field since the SPIO is within the FFL, and adiabatic response due to the low drive frequency of 1 kHz. Then, it is true that regardless of the nanoparticle density $\rho(z)$, the ratio of the 5th and 3rd higher harmonics (A_5/A_3) for a calibrated particle type k is then solely a function of the final effective drive field H_{eff} ‘felt’ by the nanoparticles (H_{eff} will encompass within it the factors of NPIC shielding and drive field weakening with z -depth).

$$R_{5th/3rd} = \frac{A_5}{A_3} = f_k(H_{\text{eff}}) \quad (4)$$

As seen in Fig. 5 panel 2, the function f_k is a well-behaved monotonically increasing function for non-zero values of H_{eff} and thus invertible for NPICs within the FOV (since shielding is never 100% and the drop-off of H_{eff} within a 7 cm depth is finite). As such, by measuring (A_5/A_3) of the MPI signal it is possible to calculate H_{eff} by taking the inverse of function f_k .

3) Calculating z-coordinate of the sole NPIC in pixel: Obtain z-coordinate from receive coil sensitivity drop-off with z-distance

NPICs have the SPIOs sealed off from the *in vivo* environment and the SPIOs only interact magnetically with MPI scanner and the sensor circuit. Thus, NPICs have a fixed and known nanoparticle density $\rho(z)$. Since the NPIC is now located along the axis of the FFL(z) and the drive field axis is along the FFL, this is a ‘zero-dimensional’ MPS measurement with background gradient field strength value $H = 0$. Thus, Equation 1 reduces to:

$$s(z) = B(z) \cdot m \cdot N \cdot \left(\frac{d\mathcal{L}(kH)}{dH} \cdot \frac{H_{\text{eff}}\omega_0}{H_{\text{sat}}} \right) \Big|_{H=0} \quad (5)$$

The MPS signal intensity $s(z)$ is thus a function of receiver sensitivity map $B(z)$ along the z -aligned FFL since the nanoparticle constant k , nanoparticle amount N [mol], ‘felt’ drive field terms in the large brackets are known. This shows that with a calibrated $B(z)$, the NPIC z -coordinate can be found by solving for z . The net effect of the drop-off of receiver sensitivity $B(z)$ and drive field amplitude with increasing z (distance of SPIO from single-sided transmitter and receiver) is plotted in Fig. 3e, and shows a maximum operating depth of 7 cm. Beyond this value the drive amplitude and receiver sensitivity of current device is too low to record the requisite signal higher harmonics.

4) Assessing the impact of NPIC sensor on SPIO i.e. shielding factor and obtaining the NPIC sensor readout value from the MPI signal

At this point, the 3D coordinate of the NPIC has been obtained with the [X,Y] coordinates from Equation 1 and 2, and the z coordinate from Equation 5. The last unknown is the sensor readout value (r) which is a parameter of the shielding factor (S) on the SPIOs within it. The FFL is fixed to be along drive coil axis and moved with drive coil to sweep the FOV. Thus

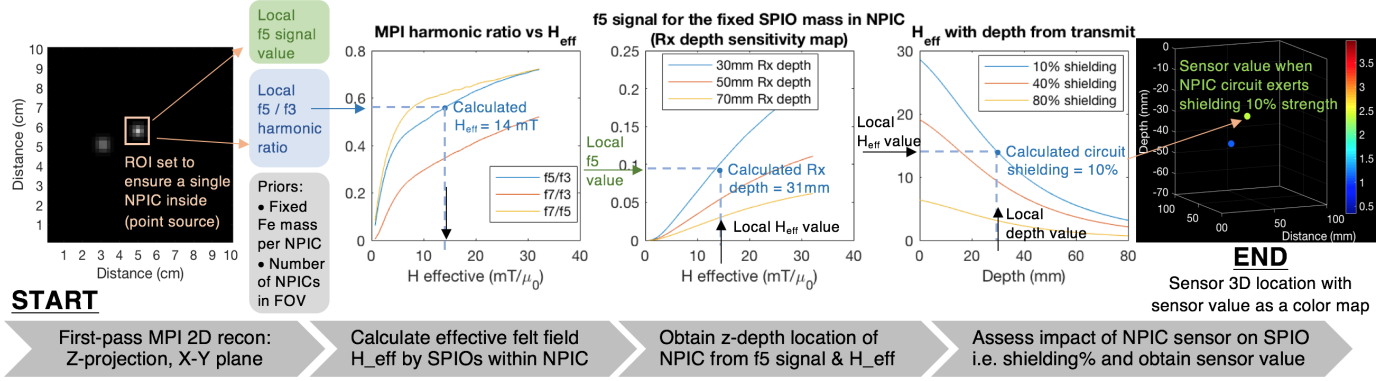


Fig. 5. Reconstruction workflow illustrated to show how the end product of a 3D volume with 4th dimension of sensor value is obtained starting from a standard MPI 2D projection scan. At the start, a first-pass MPI 2D recon is performed with a Z -projection and translation of the scanner device covering the entire XY plane, where each individual NPIC device is isolated as a single point source within its own unique regions-of-interest (ROI) to ensure no partial volume in the MPI spectral information. This concept is similar to MRI chemical shift imaging (CSI) which shifts to larger voxels than MRI anatomic scans but has all the spectral information within the voxel. In the second step, we focus on f_5/f_3 harmonic ratios which only depend on the effective applied field H_{eff} felt by SPIOs within the NPIC and are independent of SPIO distance from receiver coil (note: distance from transmit coil is accounted for by the H_{eff} value). Using the measured harmonic ratio value within the ROI, H_{eff} is back-calculated using pre-calibrated datasets since the SPIO concentration and Fe mass within each NPIC is fixed, equal and known. The third step obtains the z -coordinate or depth value of each NPIC using the measured f_5 value cross-referenced to expected f_5 values for the known SPIO concentration at calibrated H_{eff} . Any offset is due to sensitivity variations caused by the receiver's sensitivity mapping with depth, which gives us the depth value. The final step obtains the impact of the NPIC on the SPIO signal such as the strength of the NPIC shielding by comparing the measured H_{eff} against the expected H_{eff} as calibrated from the transmit sensitivity map with depth. From the circuit design, the strength of shielding corresponds to an NPIC sensor value which is then back-calculated and plotted as a color map on the final 3D location image of the array of NPICs *in vivo*.

for signal-producing nanoparticles positioned along the drive coil axis in z , the final effective drive field in z -direction, H_{eff} 'felt' by the nanoparticles from a single drive coil of radius R and amplitude H_0 at $z = 0$ is:

$$H_{\text{eff}} = S(r) \cdot H_0 \cdot \left(\frac{R^3}{(z^2 + R^2)^{3/2}} \right) \quad [S \in (0, 1)] \quad (6)$$

where $S(r)$ is the shielding factor between 0 to 1, and the bracketed term is the drop-off of drive field amplitude with depth in z . Note that for actual drive coils with multiple loops the distance drop-off term in large brackets will be a summation term of individual loops and can be solved by numerical method. For resonance-based setups, the $S(r)$ value can be larger than 1.

To complete the reconstruction for the last unknown $S(r)$, it can be solved for by substituting the known H_{eff} and the NPIC z -coordinate obtained from Step 3 and Step 4. The function $S(r)$ varies depending on the sensor but it is a monotonic well-behaved function that is generally represented by the curve shape in Fig. 8c and 8f, and thus the sensor readout value (r) can be obtained by taking the inverse function of $S(r)$.

III. METHODS

A. Magnetic Particle Imaging Device

The MPI measurements in this study were collected from an adapted design of the Berkeley Arbitrary Waveform Relaxometer, which has been modified to image for objects outside of it (compared to typical usage of inserting sample into the bore). This relaxometer design has been validated in prior work [31]–[33]. This is in conjunction with mechanical 2D motion and a permanent magnet array to establish the selection field, enabling imaging through the 2D translation

of the relaxometer body across a transparent stage platform (thin acrylic plate) that encompasses a 20 cm long \times 10 cm wide \times 10 cm deep imaging field-of-view.

B. MPI Scanning Workflow

The image reconstruction steps are detailed mathematically in the Theory section. For the actual implementation of the scan process, an ' $X - Y$ ' plane tilted at appropriate angle-to-the-vertical Z -axis is first selected. This is implemented with a thin, transparent and rigid acrylic plate with length and width dimensions of the 2D Field-of-view that is placed and secured (angle and position) on the imaging subject. This angle may be adjusted once or twice if the first MPI scan shows overlapping NPICs in the FFL projection axis. The acrylic plate angle relative to gravitational vertical was measured by a 2-Axis Vertical Precision digital spirit level (Digi-Pas DWL-1900XY). Since the flat receiver end of the MPI device is flush with the acrylic plate and translates smoothly across its surface, it ensures that the MPI device (and FFL) axis is always perpendicular to the plate and ensures a constant FFL axis angle with the gravitational vertical. A single-angle projection x-space MPI scan [38] is then performed by mechanically rastering/sliding the entire MPI FFL device comprising selection field and drive/receive coils across the acrylic plate.

Once the imaging data is acquired, the reconstruction algorithm proceeds as described in the Theory section. As our reconstruction method does not depend on reconstruction-from-projections unlike typical MPI FFL projection reconstruction methods, we simply define the tilted (corrected) angle as the new reference $X - Y$ plane and reconstruct the 3D volume with the same method used when there is zero tilt. Once 3D coordinates of the implanted devices are obtained for the tilted

reference plane, a coordinate transform step is performed to shift them to a coordinate reference with z as the gravitational vertical axis. In the case of a patient subject, the patient's body axes is also appropriately aligned to gravitational vertical axis such that the transformed 3D MPI image can be accurately superimposed on the patient body outline or MRI/CT anatomic scan.

C. Magnetic Nanoparticles (MNPs)

PerimagTM plain SPIO nanoparticles of 130 nm diameter (Micromod Partikeltechnologie GmbH, Rostock, Germany) were used in the devices. These are multi-core cluster-type particles with 70%(w/w) iron oxide in a matrix of cross-linked dextran. The nanoparticles were embedded within the implantable circuit at stock concentration of 25 mg/mL with about 10 μ L volume. Details regarding the performance and characterization of PerimagTM are detailed in prior MPI work [11].

D. Implantable Circuits

The circuit consists a basic LC resonator with a serially connected sensor or switching circuit. We wound an inductor of AWG 33 copper wires on a medical-grade silicone catheter tube. Both ends of an inductor are connected on a millimeter-scale flexible printed circuit board with capacitors and sensors (Fig. 7c). The entire implantable circuit surrounds a hollow, liquid-containing medical-grade silicon catheter tube that is fully sealed-off with biocompatible polydimethylsiloxane (PDMS). A concentrated amount of SPIO nanoparticles (or non-SPIO MNPs) can be injected into the region and sealed. Similar to most other implantable sensors/electronics [39]–[41], the device is not designed to biodegrade. Due to the long *in vivo* stability of the PDMS sealant, the MNP liquid is completely closed-off from the outside and a stable concentration can be maintained. In addition, based on our previous work with similar construction [42], [43], the device and MNPs are expected to be stable for months *in vivo*. For sensors, we used a chip NTC thermistor (NTCG 1608, TDK corporation, Japan) and thin-film resistive pressure sensor (SEN0295, DFRobot).

IV. RESULTS

A. Handheld MPI reader is able to obtain harmonic information at-depth through layers of meat tissue

Our measurements of device sensitivity with the setup illustrated in Fig. 3 show sufficient sensitivity up to 7 cm in depth. Because at least two harmonics need to be detected for our reconstruction, we are unable to utilize data when the 5th harmonic approaches the noise floor as a result of decreasing drive amplitude and receiver sensitivity both of which fall-off with distance from our handheld device. However, the sensitivity map of our current MPI receiver overlaid on a human side profile suggests that implanted sensor devices within a human such as those in the gut should still be detectable by a handheld reader if implanted within 7 cm of the front or back of the torso (Fig. 3d). Here, we have assumed a regular human male (70 kg) side profile with a torso

thickness of 20 cm for our initial proof-of-concept. Further improvements in the depth sensitivity of the receiver is needed to accommodate larger human subjects. Although our portable device is less sensitive in absolute terms than existing large-scale MPI systems, we leverage the ability to utilize highly-concentrated (25 mg/ml) nanoparticle dose concentrated into a tight point source inside the NPIC. These act like ideal point sources and therefore can still be detected even with the drop in sensitivity with depth.

B. MPI imparts 3D spatial encoding to implanted circuits via onboard SPIO nanoparticles while simultaneously extracting sensor information

Conventional near-field methods to wirelessly communicate with implanted circuits do not allow for imaging due to the wide sensitivity region of the reader and lack of spatial encoding. The results in Fig. 4 show that MPI is able to image the SPIO capsules within the implantable circuits and provide spatial encoding. Since the dimensions of each implanted device are a few mm across, it is reasonable to use a device spacing of about 1 cm as used in our demonstration. From a workflow perspective, we also demonstrate how to utilize information from the initial 2D projection scan and the known number of devices put into the FOV. It must be noted that each device is effectively an equal point source to one another due to the same dimensions and the same mass of SPIO inside. It is thus possible to robustly detect the case of multiple devices within the same Z -line (point sources counted in 2D projection image number is less than known implant count). This allows the user to select another imaging angle to ensure only one device per Z -line which is required for our reconstruction as explained in Theory Section 2D. Datasets of pre-calibrated measurements of transmit and receive sensitivity maps as well as harmonic ratios of the known SPIO masses within the device were fed into our new reconstruction algorithm illustrated in Fig. 5. From the imaging acquisition data, we were then able to successfully obtain both the 3D position as well as the sensor information as the fourth 'color' dimension.

C. An electromagnetic shielding approach is an effective way to couple biosensing readout to MPI signal

Fig. 6 demonstrates that the shielding-based strategy is able to effectively modulate the MPI signal and can be robustly extracted in image-reconstruction to reflect the level-of-shielding afforded by the sensor circuitry. There is a large amount of MPI signal change in both the relative harmonic ratios and also the total MPI signal. Since SPIOs are encapsulated within the circuit and do not decay over time, the change in total MPI signal can also correlate with the biosensing readout.

From an imaging perspective, the point-spread-function and spot size plotted in Fig. 6d,e show that there can be significant spread of the 3rd harmonic signal to the surrounding space up to a 6mm radius. Although for PerimagTM nanoparticles with a 2.8 T/m gradient, one would expect a spatial resolution closer to 3-4 mm based on the full-width-half-maximum, this is only because standard reconstruction superimposes all the higher

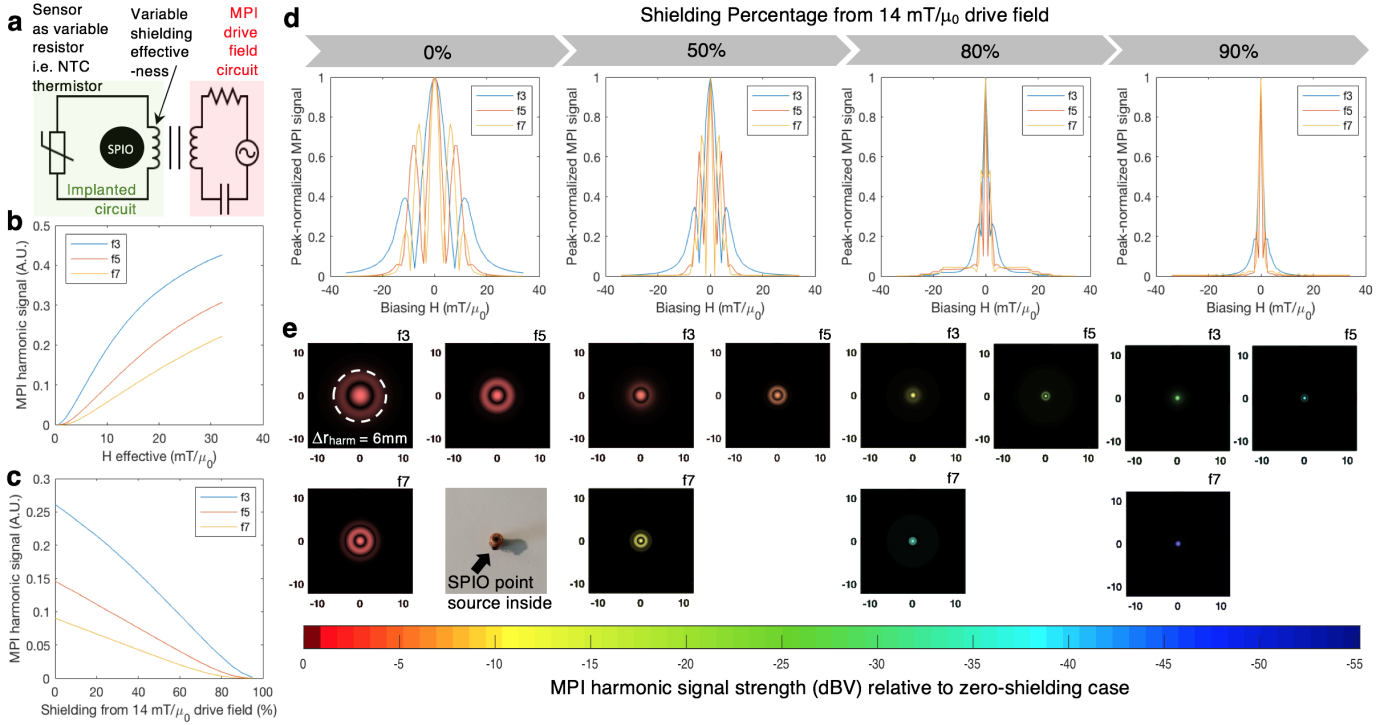


Fig. 6. Shielding-based strategy for coupling sensor information to MPI imaging information. Characterization of harmonic signal strength and 2D spatial resolution at different shielding strengths. (a) Circuit diagram illustrating how the sensor can control the shielding effectiveness via variable resistance. (b) MPI harmonic signal variation with effective applied H-field which is a direct function of the implanted circuit shielding strength. (c) MPI harmonic signal at a fixed 14 mT/ μ_0 drive field with variable implanted circuit shielding strength. (d) Measured harmonic signal strength (magnitude only, no phase) against a background biasing field to obtain the effective-1D point spread function for each harmonic for a range of different shielding values. (e) Measured 2D spot size at a 2.8 T/m gradient strength for each odd harmonic f_3 to f_7 for a range of different shielding values based on a X -space raster of the field-free-line across the 2D FOV shown in the photo. Since only the magnitude of the harmonic signal is plotted here, this indicates the 2D spread from a point source and informs the effective resolution for each harmonic f_3 to f_7 signal taken alone. Because all the implanted NPICs will have the same SPIO mass, the results with the largest spot size f_3 during zero-shielding suggest that the NPICs be spaced at least 6 mm from each other to minimize partial-voluming or spillover of MPI harmonic information between ROI of adjacent NPICs in the MPI image. The colormap indicates the drop in actual peak signal intensity in dBV as a result of shielding (images normalized to themselves for clear inspection of spot size).

harmonics to give a sharp peak. If each harmonic is measured independently in space, as is required for our harmonic-based ‘color’ and Z -coordinate reconstructions, it is essential to minimize partial-voluming of harmonic data across 2D pixels. As such, we measure the modulus harmonic signal at f_3 , f_5 and f_7 across space in a 2.8 T/m gradient to record the distance at which the harmonic signal drops to $< 20\%$ of peak, which is about 6 mm at zero-shielding case of a 14 mT/ μ_0 using concentrated PerimagTM particles. This is arguably sufficient for our context because the SPIO mass in each and every implanted device in the FOV is **equal** and thus there is no worry of large signal sources overshadowing smaller ones. Improvement can be achieved by setting the device dynamic range to be between 50 to 90% shielding which gives much narrower spot sizes as shown in Fig. 6e.

D. The resonant circuit approach to couple biosensing info to MPI readout is adequate but has poorer imaging performance

Fig. 7 demonstrates that the resonant-based strategy is able to effectively modulate the MPI signal and can be robustly extracted in image reconstruction to reflect the detuned and tuned state of the sensor circuitry. However, with a large

resonant amplification of the incident drive field, the SPIOs experience a very large effective field that can override the gradient-based spatial localization and encoding. As seen in panel e, the third harmonic 2D spot size reaches almost 10 mm in radius which will cause partial-voluming problems for devices at 1 cm or less spacing from each other. However, the large intensity change between the tuned and detuned state will be useful for facile detection of abnormal biological states that manifest as a departure from the normal tuned state, and would still work well for a binary sensor readout (abnormal vs. normal).

E. Proof-of-concept of sensing of various metrics i.e. temperature and force

The NPIC device design is compatible with a variety of sensors and we demonstrate high sensitivity with temperature, pressure, and strain sensors. From Fig. 8, we show that the shielding strategy can effectively couple NTC thermistor output into our MPI harmonic signal to extract temperature data from the MPI signal. Statistically significant changes in the $f_5:f_3$ harmonic ratio with tight error bars reflect robust readout of temperature from the MPI harmonic signal. Similarly, force data was encoded into MPI signal with a force sensor in the

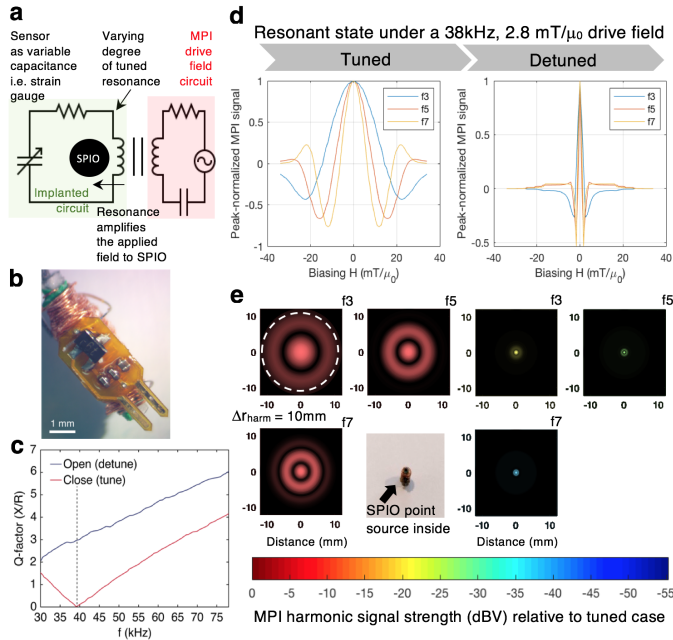


Fig. 7. Resonant-based strategy for coupling sensor information to MPI imaging information. Characterization of harmonic signal strength and 2D spatial resolution for a tuned and de-tuned circuit. (a) Circuit diagram illustrating how the sensor can control the tuned-state by variable capacitance. (b) Photo of the resonant implantable circuit. (c) Circuit response curves according to switching operation, tuned versus de-tuned. (d) Measured MPI harmonic signal strength (magnitude only, no phase) against a background biasing field to obtain the effective-1D point spread function for each harmonic at a fixed 2.8 mT/ μ_0 drive field. As resonance is expected when tuned, the drive field is set to be low. (e) Measured 2D spot size at a 2.8 T/m gradient strength for each odd harmonic f_3 to f_7 for a range of different shielding values based on a x -space raster of the field-free-line across the 2D FOV shown in the photo. The colormap indicates the drop in actual peak signal intensity in dBV as a result of loss of tuning (images normalized to themselves for clear inspection of spot size) and shows an order-of-magnitude difference in signal due to significant drive field amplification by the resonant state as opposed to the off-resonant detuned state where the nanoparticles are only excited by the low amplitude MPI drive field. There is however poorer resolution in the tuned state due to the high effective applied drive field on the nanoparticles which renders the 2.8 T/m background gradient less effective in signal localization.

circuit, with an additional open toggle switch to simulate the case of tensile rupture which will manifest as an open circuit. The results show a $\pm 0.2^\circ\text{C}$ accuracy for temperature readout in the physiological temperature range and a 1–3% error in force readout for the pressure/stress sensor.

V. DISCUSSION

A. Conventional non-imaging methods for wireless communication with implanted bioelectronic circuits

Existing work with bioelectronic implanted sensors directly communicates with the sensor via either onboard power or near-field power transmission. Typically sensors are widely-spaced apart such that the external readout device can specify the sensor by just mere proximity. Dense sensor arrays all communicating with a single external readout device would rely on frequency encoding or barcoding to identify the signal source to individual sensors, but this lacks spatial information on the sensor's exact location and will fail if the sensor moves

within the body. Prior work using a single non-imaging, near-field external reader was unable to spatially resolve adjacent sensors. For example, Kalidasan *et al.* [18] used implanted circuits to detect suture rupture and relied on modifying the suture to extend the detection range from the central implanted device. The rupture event was detected as a single binary readout from the whole area, and pinpointing of the suture rupture location was not possible. In general, conventional wireless communication methods with implanted sensors are limited to a non-imaging context.

With the addition of MPI imaging agents and encoding the bioelectronic sensor data into the MPI harmonic signal, we can harness MPI physics to provide an additional layer of spatial localization to the data transmission that is not possible with the abovementioned standard methods.

There are many real benefits that can be harnessed in this imaging context. First, we can use pre-calibrated and concentrated amounts of SPIO nanoparticles that are easier to image and reconstruct by harnessing robust priors (fixed total signal) due to the fact that MPI has zero background signal from the body and all signal must come from device nanoparticles. In addition, unlike most *in vivo* MPI imaging contexts, the entire nanoparticle dose can be highly-concentrated, safely-contained within the device and does not experience high levels of *in vivo* dilution. Since realistic biosensing applications would only have a finite number of implanted sensors and no native SPIO signal in the body, effectively, the imaging problem regresses to 3D localization of a known number of ideal, equal point sources distributed in 3D space. MPI datasets are thus favorably sparse enabling facile and rapid imaging reconstruction with minimization of image artifacts.

B. Comparison to prior work and other imaging modalities (MRI, optical, and ultrasound)

Existing non-radioactive imaging modalities such as MRI have been previously used image implanted sensors have been demonstrated [22]. However, existing imaging modalities each have their limitations (Fig. 1). Optical methods only work well for shallow implants. MRI methods heavily rely on device contrast with the tissue background, and poor contrast may result if the hypointense SPIO-device moves into a natively hypointense body region. Furthermore, susceptibility artefacts in the MRI image caused by the device can be expected. In addition, most MRI scanners are expensive and bulky unlike the portable readers typically used [18] or the handheld MPI presented in our work. Ultrasound in theory should be a strong candidate modality due to its compact, portable nature and ease-of-use. However, there are challenges in coupling existing sensors to a change in acoustic index. Furthermore, the sensors cannot be placed in regions that are acoustically shadowed by air interfaces or bone.

MPI, in contrast, suffers no such limitation as magnetic fields penetrate almost uniformly through air, bone, and tissue. MPI also has positive contrast with zero background signal and thus offers unambiguous quantitation regardless of body region which is highly desirable for implanted devices.

To our knowledge, this is the first study to investigate the use of MPI on implantable microcircuits. The shielding strategy

we used to enable the MPI signal to encode sensor data is similar in concept to the MPI saturation coil proposed in Kor et al. [44] where there is modulation of the MPI signal emanating from a selected localized region. While the method of Kor et al. proceeds by a magnetic saturation mechanism and aimed to locally suppress the unwanted MPI signal from parts of the SPIO biodistribution (liver), our method proceeds by a variable electromagnetic shielding mechanism. It modulates the amplitude of the drive field felt by the SPIO and also does not use an external saturation coil (our coil is part of the implanted microcircuit sensor).

C. Optimal MPI drive parameters for bioelectronic implant imaging

MPI uses inductive sensors such as pick-up coils thus the signal is directly proportional to the rate of change of magnetic flux [1], [30] set by the relaxation-modulated magnetization rate of the SPIO tracer. Prior work on optimization of the MPI waveform has shown two clinically-safe optima of either 70 kHz with low amplitude or 1 kHz with high amplitude waveforms [45]. In this study, we focused on the low-frequency approach (1 kHz and 38 kHz) to better match with the lower frequencies of widely used MPI hardware (0.4 kHz 20 mT/ μ_0 by Murase et al. [36] and 25 kHz 18 mT/ μ_0 by Rahmer et al. [46]).

The lower frequency also works better with superferromagnetic MPI chains which recently have been shown to possess order-of-magnitude better imaging qualities than typical SPIOs [47]–[50]. These chains have been shown to work well in organic solvents, and thus could be the imaging agent of choice in micro-scale bioelectronic implants where the microcircuit holding capsule makes the *in vivo* use of organic-immersed SPIO chains feasible. Furthermore, interesting qualities like the presence of a threshold excitation amplitude to increase signal by 100 to 1000-fold [47], [51], would have strong synergy with the shielding and resonant microcircuitry strategies towards highly-sensitive biosensors with tunable ON - OFF thresholds.

D. Suitability of Bioelectronic Components and Sensors with the MPI approach

Sensors for modulating the incoming excitation magnetic field around SPIO nanoparticles were chosen according to the mechanisms in the previous section. Amplitude modulation can be achieved by resistive sensors for measuring body temperature, pH, etc [52]. For example, because the resistance of a negative temperature coefficient (NTC) thermistor decreases as temperature rises, the current flow in the coil increases as temperature rises. As a result, the shielding effect of the coil will gradually change with temperature, and this change will be visible in the MPI image. Transistors can be used as a switching component in implementing on-off modulation, an extreme case of amplitude modulation. Bioelectrical signals flowing between the base and emitter of the transistor can appear in the MPI image due to a strong shielding effect, and bioluminescence from genetically mutated neurons also can be detected by a phototransistor with the shielding coil.

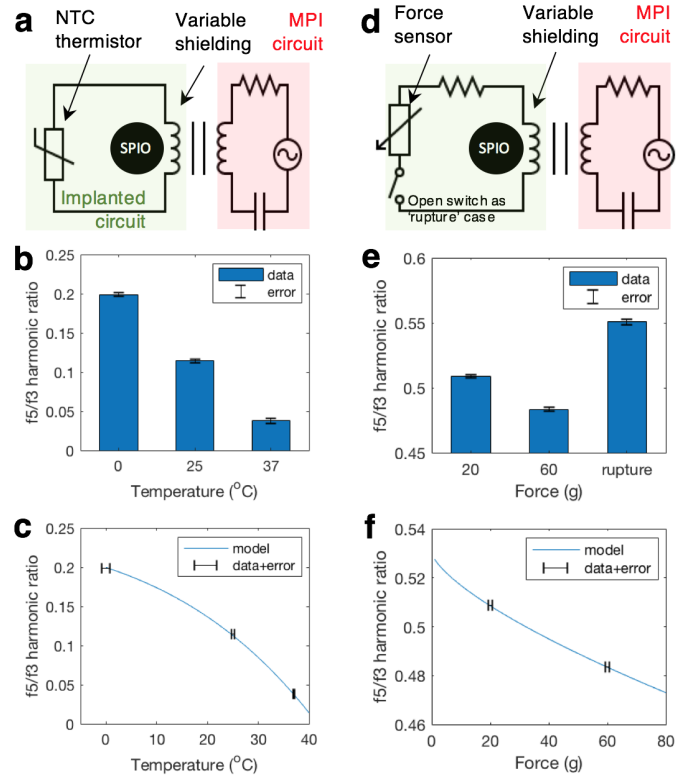


Fig. 8. Sensing of various metrics as proof-of-concept (a) Circuit diagram illustrating a temperature sensor NPIC circuit using an NTC thermistor as the key sensing element and the shielding strategy to couple sensor to MPI signal. (b) MPI harmonic measurements of the circuit at different temperatures, where the f_5/f_3 ratio changes significantly with temperature as a result of differing shielding percentages. (c) Modeled relationship between temperature and MPI harmonic ratio (f_5/f_3) calculated from NTC temperature-to-resistance curve and shielding equations. The data points with horizontal error bars indicate the achievable accuracy at different temperature zones, with ± 0.8 , 0.3 , and 0.2°C at 0, 25, and 37°C respectively. For the physiological zone around 37°C , $\pm 0.2^\circ\text{C}$ is a reasonable amount of error and can be further reduced by optimization of the circuit and NTC thermistor. (d) Circuit diagram illustrating a pressure sensor NPIC circuit using a thin film pressure sensor as the key sensing element and the shielding strategy to couple sensor to MPI signal. A switch is added to simulate the case of tensile rupture which would make an open-circuit. (e) MPI harmonic measurements of the circuit at different force applied, with increasing shielding with more force. (f) Modeled relationship between force and MPI harmonic ratio (f_5/f_3) calculated from sensor force-to-resistance curves. The horizontal error bars indicate ± 0.7 g error for a 60 g measured value (about 1% error for force measurement).

We can see an amplification of excited magnetic fields as we employ resistive sensors or transistors on LC-resonant circuits. In contrast to shielding effects without resonance, increasing harmonics can be seen in the image when the resistance is reduced or the circuit is closed.

Frequency modulation is performed by capacitive sensors in an LC-resonant circuit [52]. Capacitive sensors can convert the permittivity of materials or pressure fluctuations into electric signals by detecting capacitance variations caused by changing the electrical properties of the material or the physical distance between two electrodes. We can measure biochemical variations but also physical changes in the internal body. Capacitive strain sensors, for example, attached to the surgical site, can be used to alert when the wound ruptures.

Here, we use tiny ceramic capacitors for downscaling the LC-resonant circuit. However, some capacitors, including ferroelectric materials, such as barium titanate (BaTiO_3) [53], are not suitable for use in this due to their lower stability in strong magnetic fields. The ferroelectric materials enable high capacitance in a small package, but they produce unwanted harmonics due to their non-linearly varying capacitance with field strength. Because the harmonics of ferroelectric materials can be larger than the harmonics of SPIO nanoparticles depending on their volume, we must avoid using ferroelectric-based capacitors in this study.

E. Implementation considerations for robust 3D reconstruction and sensor readout

There are many factors i.e. temperature, dilution, viscosity *in vivo* that have potential to cause *in situ* deviations from the calibration environment resulting in errors in 3D reconstruction and sensor readout. However, our unique context of imaging implantable devices and unique characteristics of MPI provides us key benefits that ensure robustness of the results: (1) a high concentration of SPIO of known iron mass is designed to be well-sealed within the NPIC thus avoiding the negative impact of any *in vivo* dilution effects; (2) the liquid composition, viscosity and concentration is kept same as calibration time because the internal SPIO chamber is designed to be fully sealed off from *in vivo* environment thus being negligibly affected by environmental changes; (3) unlike MRI, susceptibility effects (e.g. tissue-air interfaces) from anatomic differences across device implantation sites are known to have negligible impact on MPI scans [54]; lastly, (4) the implantable device is recommended to be placed at depths greater than 1 cm from the skin. Away from the skin, body temperature is known to be highly regulated and shielded from external temperature variations. Although there is some degree of spatial variability in exact temperature depending on actual anatomic site of implantation, this can be accounted for by a thermometer measurement of the temperature of the implant site, and a quick pre-calibration of device at that temperature just before the device is surgically implanted or injected.

F. Safety considerations

The MPI drive waveform can cause magnetostimulation and tissue heating (by specific absorption ratio (SAR)) and thus the excitation frequency and amplitude f_0 and H_{amp} respectively must be kept within human-safe limits [55]. For a 1kHz drive field, it is calculated that $37 \text{ mT}/\mu_0$ amplitude measured at skin-surface is the limit for the human torso when our MPI scanner/reader device is applied perpendicular to torso axis. Fig. 3e shows that this amplitude will still give enough harmonics even with magnetic drop-off with depth.

For implantable microcircuits, one concern is that to further miniaturize the capacitors and other circuit elements on the implanted circuit, a shift to higher resonant frequencies may be necessitated. However, MPI safety limits will become more stringent with higher frequencies due to SAR concerns. In this regard, the shielding-based strategy rather than the

resonant-based strategy is more flexible as it works with low frequencies.

Other than the effect of the magnetic field on biological tissue, a non-negligible heating effect on the NPIC device may occur during long periods of scanning where there is prolonged induced current in the NPIC coil. Prior MPI studies have used MPI for the imaging of interventional guidewires [15], [56], [57]. Heating effects have been reported for some catheter guidewires under MPI conditions, but it must be noted that there was extremely wide variability in heating with most catheters having negligible temperature rises which the authors attributed to different hysteresis losses due to different ferromagnetic behavior of the metal compositions [57]. MPI signal was detected in some devices without inducing any heating, indicating the production of an effect on the MPI image does not necessitate significant heating.

To minimize induced current in the coil and the corresponding heating, we have chosen to use a low frequency of 1 kHz. In addition, modifications to the scanning sequence such as a two-stage process will significantly reduce total scan time to further minimize heating. In the first stage, low drive amplitudes that induce less current/heating will be used in the initial scan which simply aims to obtain a 2D image and thus 2D pixel coordinates of the implantable devices. In the second stage to interrogate each device for depth and sensor information, higher drive amplitudes will have to be used. To minimize the heating at high drive amplitude, rather than sweep the entire FOV again, the scan trajectory will only jump to the coordinates with devices present, pinging each very briefly (< 0.2 seconds per NPIC) with the jump time having no drive field applied to allow for cooling. This therefore greatly reduces the drive field interaction with NPIC, the net amount of heating and ensures robust z-coordinate and sensor encoding by allowing for adequate cooling time between higher-amplitude interrogation of each NPIC.

G. Potential clinical use cases

While this study is still a proof-of-concept, some potential clinical use cases specifically requiring spatial information are briefly illustrated in Fig. 2. Case 1 would be to track and readout from a mobile implanted sensor, such as a pill that moves through the gastrointestinal tract. The key advantage in a clinical use case is to the ability to provide fine spatial location information for each sensor reading as it moves along the entire distance of the gastrointestinal tract. Thus, the parameter-to-measure that is of value here is an accurate 3D location of the pill. Other methods such as a 'pillcam' can only note the time and coarsely estimate its gastrointestinal location based on camera images.

Case 2 would be post-operative monitoring of deep internal surgery where an array of implantables can monitor healing, suture rupture etc. The key potential parameters to measure are (1) biochemical healing markers released as healing progresses, (2) change in pH due to gastric juices/bile leaking from suture-ruptured anastomosis and finally (3) strain or pressure-based sensing of internal swelling due to local inflammation from infection. This may help detect infection

or cancer-relapse events in a spatially-informed manner for an extended time period post-surgery.

H. Limitations of the current study

As this is a proof-of-concept study, there are several limitations of the current NPIC system: (1) imaging depth is currently limited to 7 cm which requires that the device be implanted within 7 cm from the front or back; (2) heat produced by significant current flowing in the micro-circuit is a concern for long imaging periods; (3) the current image reconstruction workflow assumes there is only one device per Z -line, which may complicate the imaging process as there is a need to adjust the angle of the FFL. Some strategies to address these practical implementation issues are: (1) imaging depth can be improved with larger receiver coils and/or better MNPs producing stronger signals such as superferromagnetic nanoparticles [47] that have 20-fold stronger signal per iron mass ; (2) optimizing the MPI scan strategy by using lower drive amplitude MPI that minimizes induced current and heating in NPIC for a first-pass imaging to locate all the microdevices in a 2D projection plane, saving the spatial coordinates, then only jumping to those coordinates to interrogate for sensor value. This is opposed to having the scan trajectory cover the entire 2D projection plane at high drive amplitude ; (3) The time taken to “converge” to an appropriate imaging angle of the FFL can be reduced to a minimal number of iterations by utilizing prior knowledge of how many NPICs were implemented and the initial scan to calculate and recommend an angle to try. Inherently, MPI has a sparse imaging context as there is only signal from the SPIOs in the implanted devices with zero signal from biological tissue, making it easier to quickly identify an appropriate imaging angle. Furthermore, this limitation to find the imaging angle is also present in clinically used modalities like ultrasound, where the operator may have to change the angle of imaging to find the acoustic window. As such, if the appropriate imaging angle can be quickly found with minimal iterations, this limitation may be considered acceptable when viewed alongside current clinical imaging workflows.

VI. CONCLUSION

In this work, we show that implantable coil-based transducers that are detectable via MPI can be imaged as an array to spatially distinguish the bioelectronic signal from different implants to enable the remote sensing of biological metrics in a spatially distributed manner. These devices consist of inductively coupled resonant circuits that change their properties in response to electrical, thermal or photonic cues, thereby modulating the local magnetic particle imaging signal without the need for onboard power. We demonstrate modification of the MPI imaging technique to extract both spatial information as well as other information transmitted by the implanted circuit (for example, biosensing) encoded in the magnetic particle spectrum and presented as a changing color tone with a variable biometric. Biophysical sensing via bioelectronic circuits that leverage the tracer-like imaging properties of MPI may enable a wide range of minimally invasive applications in biomedicine and diagnosis.

ACKNOWLEDGMENT

The authors gratefully acknowledge grants from the Agency of Science, Technology and Research (A*STAR) under its BMRC Central Research Fund (UIBR, Z.W. Tay, M. Olivo), Career Development Fund 202D800036, and National Medical Research Council Open Fund Young Individual Research Grant (OFYIRG21nov-0044). This work was partly supported by the National Research Foundation of Korea (NRF) grant funded by the Korea government (MSIT) (RS-2023-00214390).

REFERENCES

- [1] B. Gleich and J. Weizenecker, “Tomographic imaging using the nonlinear response of magnetic particles,” *Nature*, vol. 435, pp. 1214–1217, 2005.
- [2] J. Rahmer, J. Weizenecker, B. Gleich, and J. Borgert, “Signal encoding in magnetic particle imaging: properties of the system function,” *BMC Med. Imaging*, vol. 9, p. 4, 1 Apr. 2009.
- [3] M. Graeser, T. Knopp, P. Szwargulski, T. Friedrich, A. von Gladiss, and M. Kaul et al., “Towards picogram detection of superparamagnetic Iron-Oxide particles using a gradiometric receive coil,” *Sci. Rep.*, vol. 7, no. 1, p. 6872, Jul. 2017.
- [4] P. Chandrasekharan, Z. W. Tay, X. Y. Zhou, E. Yu, R. Orendorff, and D. Hensley et al., “A perspective on a rapid and radiation-free tracer imaging modality, magnetic particle imaging, with promise for clinical translation,” *Br. J. Radiol.*, vol. 91, no. 1091, p. 20180326, Nov. 2018.
- [5] B. Zheng, T. Vazin, P. Goodwill, A. Conway, A. Verma, and E. Saritas et al., “Magnetic particle imaging tracks the long-term fate of in vivo neural cell implants with high image contrast,” *Sci. Rep.*, vol. 5, p. 14055, 11 Sep. 2015.
- [6] T. Knopp, N. Gdaniec, and M. Möddel, “Magnetic particle imaging: from proof of principle to preclinical applications,” *Phys. Med. Biol.*, vol. 62, no. 14, pp. R124–R178, Jun. 2017.
- [7] B. Zheng, E. Yu, R. Orendorff, K. Lu, J. J. Konkole, and Z. W. Tay et al., “Seeing SPIOs directly in vivo with magnetic particle imaging,” *Mol. Imaging. Biol.*, vol. 19, no. 3, pp. 385–390, Jun. 2017.
- [8] E. Y. Yu, M. Bishop, B. Zheng, R. M. Ferguson, A. P. Khandhar, and S. J. Kemp et al., “Magnetic particle imaging: A novel in vivo imaging platform for cancer detection,” *Nano Lett.*, vol. 17, no. 3, pp. 1648–1654, Mar. 2017.
- [9] E. Y. Yu, P. Chandrasekharan, R. Berzon, Z. W. Tay, X. Y. Zhou, and A. P. Khandhar et al., “Magnetic particle imaging for highly sensitive, quantitative, and safe in vivo gut bleed detection in a murine model,” *ACS Nano*, vol. 11, no. 12, pp. 12067–12076, Dec. 2017.
- [10] X. Y. Zhou, K. E. Jeffris, E. Y. Yu, B. Zheng, P. W. Goodwill, P. Nahid, and S. M. Conolly, “First in vivo magnetic particle imaging of lung perfusion in rats,” *Phys. Med. Biol.*, vol. 62, no. 9, pp. 3510–3522, May 2017.
- [11] Z. W. Tay, P. Chandrasekharan, X. Y. Zhou, E. Yu, B. Zheng, and S. Conolly, “In vivo tracking and quantification of inhaled aerosol using magnetic particle imaging towards inhaled therapeutic monitoring,” *Theranostics*, vol. 8, no. 13, pp. 3676–3687, 2018.
- [12] P. Ludewig, N. Gdaniec, J. Sedlacik, N. D. Forkert, P. Szwargulski, and M. Graeser et al., “Magnetic particle imaging for Real-Time perfusion imaging in acute stroke,” *ACS Nano*, vol. 11, no. 10, pp. 10480–10488, Oct. 2017.
- [13] R. Orendorff, A. J. Peck, B. Zheng, S. N. Shirazi, R. Matthew Ferguson, and A. P. Khandhar et al., “First in vivo traumatic brain injury imaging via magnetic particle imaging,” *Phys. Med. Biol.*, vol. 62, no. 9, pp. 3501–3509, 7 May 2017.
- [14] S. Vaalma, J. Rahmer, N. Panagiotopoulos, R. L. Duschka, J. Borgert, and J. Barkhausen et al., “Magnetic particle imaging (MPI): Experimental quantification of vascular stenosis using stationary stenosis phantoms,” *PLoS One*, vol. 12, no. 1, p. e0168902, 5 Jan. 2017.
- [15] J. Rahmer, D. Wirtz, C. Bontus, J. Borgert, and B. Gleich, “Interactive magnetic catheter steering with 3-D Real-Time feedback using Multi-Color magnetic particle imaging,” *IEEE Trans. Med. Imaging*, vol. 36, no. 7, pp. 1449–1456, Jul. 2017.
- [16] D. Hensley, Z. W. Tay, R. Dhavalikar, B. Zheng, P. Goodwill, and C. Rinaldi et al., “Combining magnetic particle imaging and magnetic fluid hyperthermia in a theranostic platform,” *Phys. Med. Biol.*, vol. 62, no. 9, pp. 3483–3500, May 2017.

- [17] Z. W. Tay, P. Chandrasekharan, A. Chiu-Lam, D. W. Hensley, R. Dhavalikar, and X. Y. Zhou *et al.*, "Magnetic particle Imaging-Guided heating in vivo using localized fields for arbitrary localization of magnetic hyperthermia therapy," *ACS Nano*, vol. 12, no. 4, pp. 3699–3713, Apr. 2018.
- [18] V. Kalidasan, X. Yang, Z. Xiong, R. R. Li, H. Yao, H. Godaba, S. Obuobi, P. Singh, X. Guan, X. Tian *et al.*, "Wirelessly operated bioelectronic sutures for the monitoring of deep surgical wounds," *Nat. Biomed. Eng.*, vol. 5, no. 10, pp. 1217–1227, 2021.
- [19] S. Kim, J. Malik, J. M. Seo, Y. M. Cho, and F. Bien, "Subcutaneously implantable electromagnetic biosensor system for continuous glucose monitoring," *Sci. Rep.*, vol. 12, no. 1, p. 17395, 2022.
- [20] M. M. Ahmadi and G. A. Jullien, "A wireless-implantable microsystem for continuous blood glucose monitoring," *IEEE T. BIOMED. CIRC. S.*, vol. 3, no. 3, pp. 169–180, 2009.
- [21] A. Singer and J. T. Robinson, "Wireless power delivery techniques for miniature implantable bioelectronics," *Adv. Healthc. Mater.*, vol. 10, no. 17, p. 2100664, 2021.
- [22] A. Hai, V. C. Spanoudaki, B. B. Bartelle, and A. Jasanoff, "Wireless resonant circuits for the minimally invasive sensing of biophysical processes in magnetic resonance imaging," *Nat. Biomed. Eng.*, vol. 3, no. 1, pp. 69–78, 2019.
- [23] Z. Li, K. Wang, C. Hou, C. Li, F. Zhang, W. Ren, L. Dong, and J. Zhao, "Self-sensing intelligent microrobots for noninvasive and wireless monitoring systems," *Microsyst. Nanoeng.*, vol. 9, no. 1, p. 102, 2023.
- [24] R. C. Susil, C. J. Yeung, H. R. Halperin, A. C. Lardo, and E. Atalar, "Multifunctional interventional devices for MRI: a combined electrophysiology/MRI catheter," *Magn. Reson. Med.*, vol. 47, no. 3, pp. 594–600, Mar. 2002.
- [25] M. B. Bilgin, M. E. Tiryaki, J. Lazovic, and M. Sitti, "Radio frequency sensing-based in situ temperature measurements during magnetic resonance imaging interventional procedures," *Adv. Mater. Technol.*, vol. 7, no. 9, p. 2101625, 2022.
- [26] M. N. Gulari, M. Ghannad-Rezaie, P. Novelli, N. Chronis, and T. C. Marentis, "An implantable x-ray-based blood pressure microsensor for coronary in-stent restenosis surveillance and prevention," *J. Microelectromech. Syst.*, vol. 24, no. 1, pp. 50–61, 2014.
- [27] S. D. Kiridena, U. N. Wijayarathna, E. Levon, P. Moschella, R. G. Pirrallo, T.-R. J. Tzeng, and J. N. Anker, "X-ray visualized sensors for peritoneal dialysis catheter infection," *Adv. Funct. Mater.*, p. 2204899, 2023.
- [28] Z. W. Tay, P. Chandrasekharan, B. D. Fellows, I. R. Arrizabalaga, E. Yu, M. Olivo, and S. M. Conolly, "Magnetic particle imaging: An emerging modality with prospects in diagnosis, targeting and therapy of cancer," *Cancers*, vol. 13, no. 21, p. 5285, Oct. 2021.
- [29] T. Knopp, S. Biederer, T. F. Sattel, M. Erbe, and T. M. Buzug, "Prediction of the spatial resolution of magnetic particle imaging using the modulation transfer function of the imaging process," *IEEE Trans. Med. Imaging*, vol. 30, no. 6, pp. 1284–1292, Jun. 2011.
- [30] P. W. Goodwill and S. M. Conolly, "The x-space formulation of the magnetic particle imaging process: 1-d signal, resolution, bandwidth, snr, sar, and magnetostimulation," *IEEE Trans. Med. Imaging*, vol. 29, no. 11, pp. 1851–1859, 2010.
- [31] Z. W. Tay, P. W. Goodwill, D. W. Hensley, L. A. Taylor, B. Zheng, and S. M. Conolly, "A High-Throughput, Arbitrary-Waveform, MPI spectrometer and relaxometer for comprehensive magnetic particle optimization and characterization," *Sci. Rep.*, vol. 6, p. 34180, Sep. 2016.
- [32] Z. W. Tay, D. W. Hensley, E. C. Vreeland, B. Zheng, and S. M. Conolly, "The relaxation wall: Experimental limits to improving MPI spatial resolution by increasing nanoparticle core size," *Biomed. Phys. Eng. Express*, vol. 3, no. 3, pp. 035003–035003, Jun. 2017.
- [33] Z. W. Tay, D. Hensley, J. Ma, P. Chandrasekharan, B. Zheng, P. Goodwill, and S. Conolly, "Pulsed excitation in magnetic particle imaging," *IEEE Trans. Med. Imaging*, vol. 38, no. 10, pp. 2389–2399, Oct. 2019.
- [34] P. W. Goodwill, K. Lu, B. Zheng, and S. M. Conolly, "An x-space magnetic particle imaging scanner," *Rev. Sci. Instrum.*, vol. 83, no. 3, p. 033708, Mar. 2012.
- [35] K. Grafe, A. von Gladiss, G. Bringout, M. Ahlberg, and T. M. Buzug, "2D images recorded with a Single-Sided magnetic particle imaging scanner," *IEEE Trans. Med. Imaging*, vol. 35, no. 4, pp. 1056–1065, Apr. 2016.
- [36] K. Murase, S. Hiratsuka, R. Song, and Y. Takeuchi, "Development of a system for magnetic particle imaging using neodymium magnets and gradiometer," *Jpn. J. Appl. Phys.*, vol. 53, no. 6, p. 067001, 2014.
- [37] N. Löwa, P. Radon, O. Kosch, and F. Wiekhorst, "Concentration dependent MPI tracer performance," *Int J Mag Part Imag*, vol. 2, no. 1, Jan. 2016.
- [38] P. W. Goodwill, J. J. Konkole, B. Zheng, E. U. Saritas, and S. M. Conolly, "Projection x-space magnetic particle imaging," *IEEE Trans. Med. Imaging*, vol. 31, no. 5, pp. 1076–1085, May 2012.
- [39] I. Miranda, A. Souza, P. Sousa, J. Ribeiro, E. M. Castanheira, R. Lima, and G. Minas, "Properties and applications of pdms for biomedical engineering: A review," *J. Funct. Biomater.*, vol. 13, no. 1, p. 2, 2021.
- [40] S.-J. Kim, D.-S. Lee, I.-G. Kim, D.-W. Sohn, J.-Y. Park, B.-K. Choi, and S.-W. Kim, "Evaluation of the biocompatibility of a coating material for an implantable bladder volume sensor," *Kaohsiung J. Med. Sci.*, vol. 28, no. 3, pp. 123–129, 2012.
- [41] R. Carta, P. Jourand, B. Hermans, J. Thoné, D. Brosteaux, T. Vervust, F. Bossuyt, F. Axisa, J. Vanfleteren, and R. Puers, "Design and implementation of advanced systems in a flexible-stretchable technology for biomedical applications," *Sens. Actuators A. Phys.*, vol. 156, no. 1, pp. 79–87, 2009.
- [42] B. Sun, J. N. Bte Rahmat, H. J. Kim, R. Mahendran, K. Esuvaranathan, E. Chiong, J. S. Ho, K. G. Neoh, and Y. Zhang, "Wirelessly activated nanotherapeutics for in vivo programmable photodynamic-chemotherapy of orthotopic bladder cancer," *Adv. Sci.*, vol. 9, no. 16, p. 2200731, 2022.
- [43] A. Bansal, F. Yang, T. Xi, Y. Zhang, and J. S. Ho, "In vivo wireless photonic photodynamic therapy," *Proc. Nat. Acad. Sci.*, vol. 115, no. 7, pp. 1469–1474, 2018.
- [44] E. Kor, M. T. Arslan, and E. U. Saritas, "Saturation coil for localized signal suppression in MPI," *Int J Mag Part Imag*, vol. 8, no. 1, p. 2203013, 2022.
- [45] Z. W. Tay, D. W. Hensley, P. Chandrasekharan, B. Zheng, and S. M. Conolly, "Optimization of drive parameters for resolution, sensitivity and safety in magnetic particle imaging," *IEEE Trans. Med. Imaging*, vol. 39, no. 5, pp. 1724–1734, May 2020.
- [46] J. Rahmer, J. Weizenecker, B. Gleich, and J. Borgert, "Analysis of a 3-D system function measured for magnetic particle imaging," *IEEE Trans. Med. Imaging*, vol. 31, no. 6, pp. 1289–1299, Jun. 2012.
- [47] Z. W. Tay, S. Savliwala, D. W. Hensley, K. L. B. Fung, C. Colson, B. D. Fellows, X. Zhou, Q. Huynh, Y. Lu, B. Zheng, P. Chandrasekharan, S. M. Rivera-Jimenez, C. M. Rinaldi-Ramos, and S. M. Conolly, "Superferromagnetic nanoparticles enable Order-of-Magnitude resolution & sensitivity gain in magnetic particle imaging," *Small Methods*, vol. 5, no. 11, p. e2100796, Nov. 2021.
- [48] Bryan, Fellows, Fung, and others, "Optimizing magnetic particle image resolution using superferromagnetic nanoparticles modified through post-synthesis oxidation," *Int J Mag Part Imag*, vol. 8, no. 1, p. e2203050, 2022.
- [49] Fung, Colson, Bryan, Fellows, and others, "Elucidating super-resolution magnetic particle imaging: superferromagnetic remanence decay through MPI signal evolution informs super-resolution MPI scan . . .," *Int J Mag Part Imag*, vol. 8, no. 1, pp. e2203051, 2022.
- [50] Saayujya, Fung, Huynh, and others, "Computational modeling of superferromagnetism in finite-length chains of superparamagnetic iron oxide tracers for use in super-resolution magnetic particle . . .," *Int J Mag Part Imag*, vol. 8, no. 1, p. e2203052, 2022.
- [51] Z. W. Tay, S. Savliwala, D. Hensley, P. Chandrasekharan, B. Fung, C. Colson, B. Fellows, S. Rivera-Jimenez, M. Olivo, C. Rinaldi, and S. Conolly, "Superferromagnetic iron oxide: a new paradigm for color multiplex and FRET-like nanoscale 'ruler' for magnetic particle imaging," in *Colloidal Nanoparticles for Biomedical Applications XVII*, M. Osiński and A. G. Kanaras, Eds. SPIE, Mar. 2022, p. e1197704.
- [52] A. Yakovlev, S. Kim, and A. Poon, "Implantable biomedical devices: Wireless powering and communication," *IEEE Commun. Mag.*, vol. 50, no. 4, pp. 152–159, 2012.
- [53] C. Randall, R. Newnham, and L. Cross, "History of the first ferroelectric oxide, batio3," *Materials Research Institute, The Pennsylvania State University, University Park, Pa, USA*, vol. 1, 2004.
- [54] E. U. Saritas, P. W. Goodwill, L. R. Croft, J. J. Konkole, K. Lu, and B. Zheng *et al.*, "Magnetic particle imaging (MPI) for NMR and MRI researchers," *J. Magn. Reson.*, vol. 229, pp. 116–126, Apr. 2013.
- [55] E. U. Saritas, P. W. Goodwill, G. Z. Zhang, and S. M. Conolly, "Magnetostimulation limits in magnetic particle imaging," *IEEE Trans. Med. Imaging*, vol. 32, no. 9, pp. 1600–1610, 2013.
- [56] S. Herz, P. Vogel, P. Dietrich, T. Kampf, M. A. Rückert, R. Kickuth, V. C. Behr, and T. A. Bley, "Magnetic particle imaging guided Real-Time percutaneous transluminal angioplasty in a phantom model," *Cardiovasc. Intervent. Radiol.*, vol. 41, no. 7, pp. 1100–1105, Jul. 2018.
- [57] R. Duschka, H. Wojtczyk, N. Panagiotopoulos, J. Haegele, G. Bringout, T. Buzug, J. Barkhausen, and F. Vogt, "Safety measurements for heating of instruments for cardiovascular interventions in magnetic particle imaging (MPI) - first experiences," *J. Healthc. Eng.*, vol. 5, no. 1, pp. 79–94, 2014.